Quantum Hall studies of a semi-Dirac nanoribbon

Priyanka Sinha,[1,*] Shuichi Murakami,[2,†] and Saurabh Basu[1,‡]
[1]*Department of Physics, Indian Institute of Technology Guwahati, Guwahati 781039, Assam, India*
[2]*Department of Physics, Tokyo Institute of Technology, 2-12-1 Ookayama, Meguro-ku, Tokyo 152-8551, Japan*

(Received 28 May 2020; accepted 22 July 2020; published 14 August 2020)

Here we comprehensively investigate Landau levels, Hofstadter's butterfly, and transport properties of a semi-Dirac nanoribbon in a perpendicular magnetic field using a recently developed real-space implementation of the Kubo formula based on the kernel polynomial method. A Dirac ribbon is considered to compare and contrast our results for a semi-Dirac system. We find that with the Landau levels being nonequidistant from each other for the semi-Dirac case (which is true for a Dirac case as well), the flatness of the energy bands vanishes in the bulk and becomes dispersive for a semi-Dirac ribbon in contrast to a Dirac system. This feature is most discernible for intermediate values of the external field. We further compute the longitudinal (σ_{xx} and σ_{yy}) and the transverse or Hall (σ_{xy}) conductivities, where the Hall conductivity shows a familiar quantization, namely, $\sigma_{xy} \propto 2n$ (the factor of 2 includes the spin degeneracy), which is highly distinct from a Dirac system, such as graphene. We also observe anisotropic behavior in magnetotransport in a semi-Dirac ribbon owing to the dispersion anomalies in two different longitudinal directions. Our studies may have important ramifications for monolayer phosphorene.

DOI: 10.1103/PhysRevB.102.085416

I. INTRODUCTION

In the past few decades, graphene has attracted much attention due to its peculiar dispersion relation at low energies, similar to the spectrum of relativistic particles described by the Dirac theory [1,2]. More precisely, the spectrum has two cones, the so-called Dirac cones in the vicinity of two nonequivalent points, K_1 and K_2, in the reciprocal space. Anisotropy in graphene was another interesting aspect which was discussed long ago by Pauling [3] and could be induced by uniaxial stress or bending of a graphene sheet. The main motive is to tune the hopping energy between neighboring carbon atoms with precision, which was later found to be feasible in optical lattices [4] via controlling the lattice potential in order to get a handle on the effective mass in a honeycomb lattice. In a tight-binding model for graphene, if one of the three nearest-neighbor hopping energies is tuned, the two Dirac points with opposite chiralities approach each other and merge into one, forming the so-called semi-Dirac point. The band dispersion simultaneously exhibits massless Dirac (linear) and massive fermionic (quadratic) features along two different directions, thereby producing a highly anisotropic electronic dispersion [5,6]. The materials that host such anisotropic dispersion are phosphorene under pressure and doping [7,8], electric fields [9,10], TiO_2/VO_2 superlattices [6,11,12], graphene under deformation [13], and quasi-two-dimensional organic conductor α-$(BEDT\text{-}TTF)_2I_3$ salt under pressure [14,15]. Experimentally, semi-Dirac dispersion has been observed in a few-layer black phosphorene by means of the *in situ* deposition of potassium atoms [16]. A straightforward approach to realize semi-Dirac materials can be achieved by breaking the hexagonal symmetry of the honeycomb lattice, e.g., by strain. However, directly applying strain to realize the transition in materials, such as graphene or silicene, is prohibited by the exorbitant magnitude of the strain required, which would eventually disintegrate them [17,18]. Some successfully synthesized graphenelike honeycomb materials, such as silicene [19,20], germanene [21], and stanene [22], have been found to be easily oxidized, or they chemically absorb other atoms because of their buckling geometries [23–26]. It is these absorbed atoms that will modify the hopping energies in the honeycomb lattice which is essentially applying a strain that creates a differential hopping. On the other hand, behaviors of electrons in graphene exposed to a strong perpendicular magnetic field played an important role not only in the discovery of the room-temperature half-integer quantum Hall effect [27–30] but also in proving the existence of massless Dirac particles [31]. The unconventional Hall conductivity was found to be quantized as $\sigma_{xy} = 2(2n+1)e^2/h$ [29,31], where both the spin and valley degeneracies are taken into account. Experimental measurements confirm that the Landau levels of a monolayer graphene obey the relation $E_n = \mathrm{sgn}(n)\sqrt{2\hbar v_F e|n|B}$, where $v_F = 10^6$ m/s is the Fermi velocity, B is the magnetic field, and n denotes Landau level indices [32,33].

Recently, quite a few studies on Landau levels and transport properties in the presence of a magnetic field in phosphorene have been reported [34,35]. More precisely, they have found that the anisotropic band structure that leads to Hall quantization in the presence of a perpendicular magnetic field is similar to that of a conventional two-dimensional electron gas (2DEG). Since phosphorene may be considered a realistic material that possesses semi-Dirac properties, it is necessary

*sinhapriyanka2016@iitg.ac.in
†murakami@stat.phys.titech.ac.jp
‡saurabh@iitg.ac.in

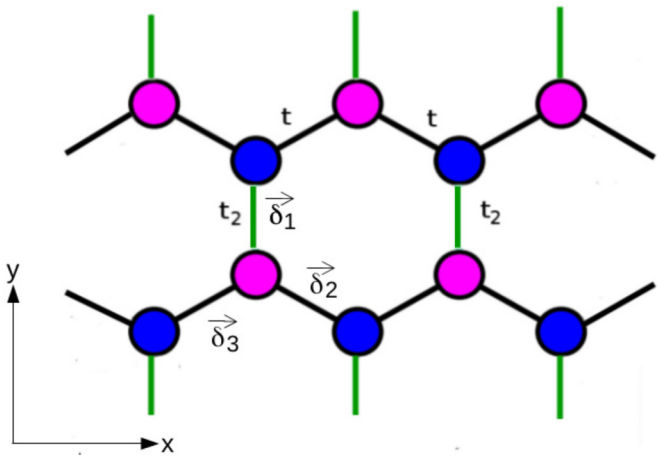

FIG. 1. A schematic diagram of the hexagonal lattice geometry of a semi-Dirac system with different hopping parameters t and t_2 is shown. Black corresponds to hopping t, whereas green corresponds to t_2. Two sublattices are denoted by two different colors (blue and magenta). $\vec{\delta}_1$, $\vec{\delta}_2$, and $\vec{\delta}_3$ are the nearest-neighbor real-space vectors.

to pursue quantum Hall studies on semi-Dirac systems. As discussed above, the energy dispersion of phosphorene is similar to that of semi-Dirac systems, and it is likely that other properties also show similar characteristics.

In this work, we explore the influence of magnetic field on a semi-Dirac system using a tight-binding Hamiltonian on a honeycomb lattice. We study the Landau level spectrum and Hofstadter's butterfly using a nanoribbon in order to show that the semi-Dirac system has properties quite distinct from Dirac fermions. We also calculate the density of states (DOS) via the tight-binding propagation method [36,37], which is a sophisticated numerical tool used in large-scale calculations for any realistic system. We have implemented the recently developed real-space order-N quantum transport approach to calculate the Kubo conductivities as a function of the Fermi energy for moderate as well as very high values of the magnetic field [38]. The Hall conductivity in a semi-Dirac system shows the *standard* quantization, namely, $\sigma_{xy} \propto 2n$, compared to the previously observed *anomalous* quantization, that is, $\sigma_{xy} \propto 4(n + 1/2)$ for a Dirac system. The longitudinal conductivities show highly anisotropic behavior in one direction compared to the other, which is obviously absent in Dirac systems.

This paper is organized as follows. The low-energy tight-binding Hamiltonian is described in Sec. II. We further study the Landau level spectra and the Hofstadter's butterfly for a nanoribbon in the presence of a magnetic field in Sec. III. The transport properties are investigated by computing the Hall and longitudinal conductivities in Sec. IV. We conclude with a brief summary in Sec. V.

II. MODEL HAMILTONIAN

We study the tight-binding model on a honeycomb lattice with anisotropic hopping that leads to semi-Dirac electronic spectra at low energy. More precisely, the hopping energy to one of the neighbors (t_2) is different from the other two (t), as shown in Fig. 1. It is also instructive to look at the full dispersion with the following three nearest-neighbor vectors in real space: $\vec{\delta}_1 = (0, a)$, $\vec{\delta}_2 = (\frac{\sqrt{3}a}{2}, -\frac{a}{2})$, and $\vec{\delta}_3 = (-\frac{\sqrt{3}a}{2}, -\frac{a}{2})$, where a is the lattice constant.

The dispersion relation for a semi-Dirac system can be written as

$$E(k) = \pm\sqrt{2t^2 + t_2^2 + 2t^2\cos\sqrt{3}k_x a + 4tt_2\cos(3k_y a/2)\cos(\sqrt{3}k_x a/2)}. \quad (1)$$

The above expression is plotted in Fig. 2(a). The Brillouin zone with high-symmetry points for $t_2 = t$ is shown in Fig. 2(b). For the Dirac case (that is, $t_2 = t$), the dispersion shows that the Dirac points touch at the K_1 and K_2 points at the Brillouin zone corners, as shown in Fig. 2(c). With increasing the strength of the parameter t_2, the two Dirac points originally located at K_1 $(\frac{2\pi}{3a}, \frac{2\pi}{\sqrt{3}a})$ and K_2 $(-\frac{2\pi}{3a}, \frac{2\pi}{\sqrt{3}a})$ move closer until they merge at the M point, resulting in a semi-Dirac spectrum [see Fig. 2(d)]. As mentioned earlier, such manipulation of the Dirac points and their eventual merger have been achieved in honeycomb optical lattices [4]. Thus, by fixing $t_2 = 2t$ and focusing on the M point $(0, \frac{2\pi}{\sqrt{3}a})$, the low-energy effective Hamiltonian based on the tight-binding model for a semi-Dirac system, apart from a constant term, can be written as [39–41]

$$H_0 = \frac{p_x^2\sigma_x}{2m^*} + v_F p_y\sigma_y, \quad (2)$$

where p_x and p_y are the momenta along the x and the y directions, respectively. σ_x and σ_y are the Pauli spin matrices in the pseudospin space. The velocity along the p_y direction v_F and the effective mass m^* corresponding to the parabolic dispersion along p_x are expressed as $v_F = 3ta/\hbar$ and $m^* = 2\hbar/3ta^2$. Henceforth, we set $a = 1$. The dispersion relation corresponding to Eq. (2) ignoring a constant shift in energy can be written as

$$E = \pm\sqrt{(\hbar v_F k_y)^2 + \left(\frac{\hbar^2 k_x^2}{2m^*}\right)^2}, \quad (3)$$

where the plus sign denotes the conduction band and the minus sign stands for the valence band. Equation (3) shows that the dispersion is linear (Dirac-like) along the y direction, whereas the dispersion along the x direction is quadratic (nonrelativistic), the combination of which results in the semi-Dirac dispersion. The three-dimensional plot in Fig. 2(a) indicates the anisotropic band structure in a semi-Dirac system.

III. THE LANDAU LEVELS

To include a magnetic field, we shall work with a semi-Dirac nanoribbon which is infinitely long along x but has a finite width along y. We apply a uniform magnetic field

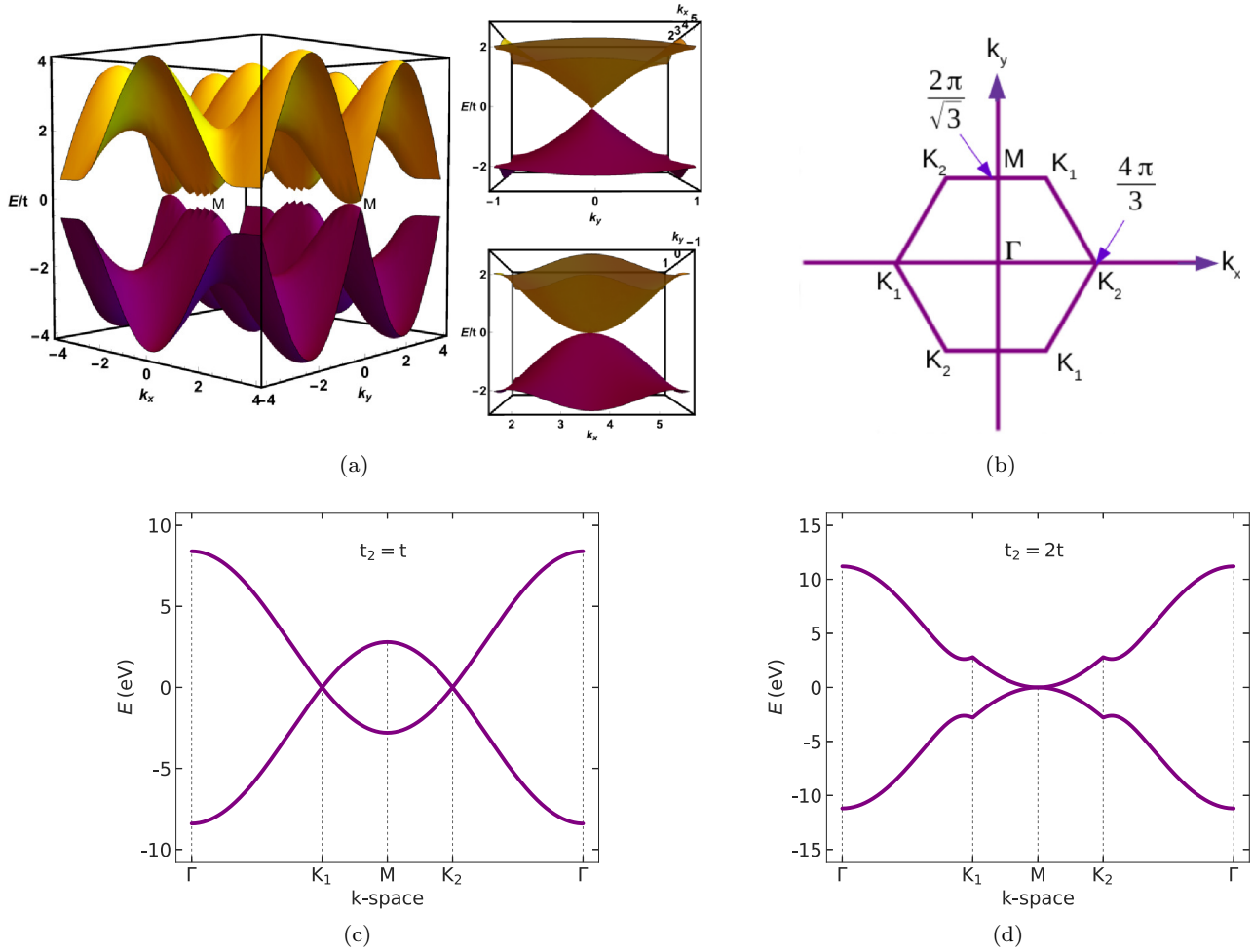

FIG. 2. (a) The anisotropic energy band dispersion of a semi-Dirac system is shown. In the side panel, we zoom in on the region near the M point along the k_y and k_x directions. The dispersion is linear along the y direction and quadratic along the x direction. Here a is set to be unity. (b) A Brillouin zone with different high-symmetry points is shown for the Dirac case. (c) and (d) The dispersion along the high-symmetry points $\Gamma \rightarrow K_1 \rightarrow M \rightarrow K_2 \rightarrow \Gamma$ for different strengths of hopping parameters $t_2 = t$ (Dirac) and $t_2 = 2t$ (semi-Dirac), respectively. Here we set $t = 2.8\,\mathrm{eV}$.

$\mathbf{B} = B\hat{z}$ perpendicular to the plane of the ribbon. Owing to the presence of the vector potential $\vec{A}$, each tight-binding wave function picks up an extra phase term. We have chosen the Landau gauge to be $\vec{A} = (-By, 0, 0)$ such that the translational invariance along the x direction remains unaltered under the choice of the gauge. Hence, the momentum along the x direction is conserved and acts as a good quantum number. To make k_x a dimensionless quantity, we have absorbed the lattice spacing a into the definition of k_x. The ribbon width is such that it has N unit cells along the y axis (where the index n for the unit cells takes $\in 0, \ldots, N-1$), as shown in Fig. 3. The tight-binding Hamiltonian in the presence of magnetic field has the form

$$H = -\sum_{\langle ij \rangle} (t_{ij} a_i^\dagger b_j + \text{H.c.}), \tag{4}$$

where $a_i^\dagger$ (b_j) creates (annihilates) an electron on sublattice A (B). t_{ij} is the hopping amplitude between nearest-neighbor sites, which obtain a phase due to the magnetic field by the Peierls substitution, namely, $t_{ij} = t \rightarrow t e^{2i\pi\phi_{ij}}$ (here t denotes both t and t_2). ϕ_{ij} is the magnetic flux and is given by the line integral of the vector potential from site i to site j, namely, $\phi_{ij} = e/h \int_i^j \vec{A} \cdot d\vec{l}$. The flux is usually denoted in terms of the flux quantum $\phi_0 = h/e$ (h is Planck's constant, and e is the magnitude of the electron charge). Thus, the tight-binding Hamiltonian in the presence of the perpendicular magnetic field can be written in terms of m and n (where m increases along the x direction and n increases along the negative y direction; see Fig. 3) [2],

$$\begin{aligned} \mathcal{H} = -\sum_{\langle mn \rangle} \big[& t e^{i\pi(\phi/\phi_0)n[(1+\alpha)/2]} a^\dagger(m,n) b(m,n) \\ & + t e^{-i\pi(\phi/\phi_0)n} a^\dagger(m,n) b(m-1, n-(1-\alpha)/2) \\ & + t_2\, e^{i\pi(\phi/\phi_0)n[(\alpha-1)/2]} a^\dagger(m,n) b(m, n-\alpha) + \text{H.c.} \big], \end{aligned} \tag{5}$$

where the summation $\langle mn \rangle$ is over the nearest neighbors. $a^\dagger(m,n)$ and $b(m,n)$ denote the creation and annihilation operators at the (m,n) site, respectively. $\alpha = 1$ can be used for a zigzag semi-Dirac nanoribbon. Using the above Hamiltonian in Eq. (5), we numerically calculated the Hofstadter's

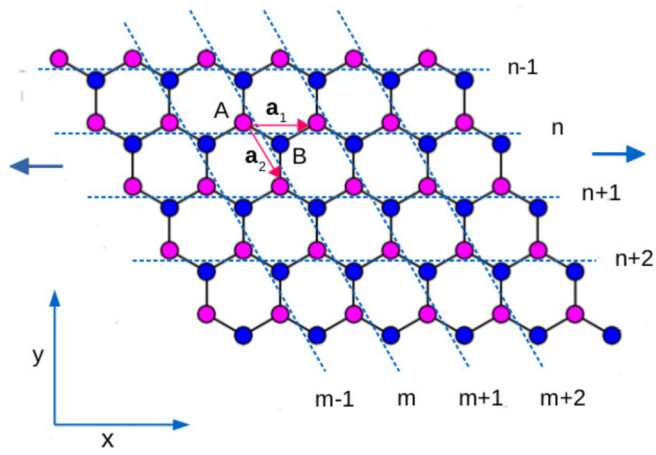

FIG. 3. The zigzag nanoribbon of a honeycomb lattice is shown. The magenta and blue circles represent the A and B sublattices, respectively. $\vec{a}_1$ and $\vec{a}_2$ are the primitive vectors. (m, n) labels the positions of the unit cells along the x and y directions. The ribbon is infinite along the x direction, shown by the arrow on both sides.

butterfly [42] as well as the Landau level spectrum for the number of unit cells $N = 100$. Figure 4(a) shows fractal spectra plotted as a function of magnetic flux ϕ/ϕ_0 for a semi-Dirac nanoribbon. It can be seen clearly that an opening of a central gap with a flat band at zero energy occurs. The gap gets larger along with the two identical spectra that emerge from the conduction and valence bands by tuning t_2. For comparison, the same is plotted for the Dirac system ($t_2 = t$), as shown in Fig. 4(b). We can see that there is no gap at zero energy with the flat band when one goes from $t_2 = 2t$ to $t_2 = t$. Figure 5 shows the Landau level spectra for different values of the magnetic flux (such as $\phi/\phi_0 = 1/100, 1/200, 1/500, 1/1600$) for the semi-Dirac and Dirac systems. Figures 5(a)–5(d) show the evolution of the energy levels in the presence of the magnetic field for a semi-Dirac nanoribbon ($t_2 = 2t$). For comparison, we have also plotted the Landau level spectrum for the Dirac case ($t_2 = t$) using the same values of the magnetic flux as shown in Figs. 5(e)–5(h). It should be noted that in a semi-Dirac system, there is no zero-energy bulk state, which implies that the zero-energy state in Fig. 5 is an edge state. On the other hand, zero-energy bulk states exist in a Dirac system. Further, for $t_2 = 2t$, the Landau levels are not equidistant since

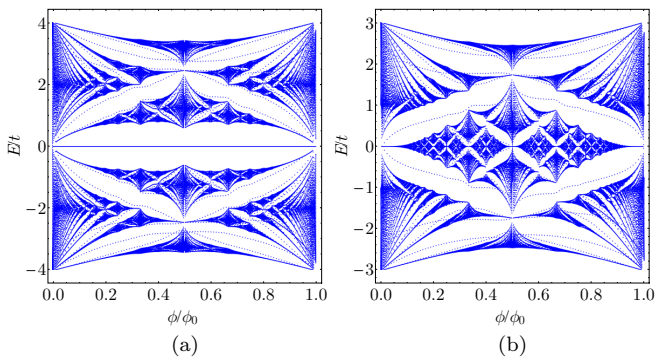

FIG. 4. The Hofstadter's butterfly spectrum is plotted as a function of ϕ/ϕ_0 for (a) $t_2 = 2t$ (semi-Dirac) and (b) $t_2 = t$ (Dirac).

their energies vary as $(n + \frac{1}{2})^{2/3}$ (with n being the Landau level index) [6], which is intermediate to the behavior of the Dirac system and the conventional 2DEG. As a consequence, the gap between the Landau levels shrinks as one considers larger n. In the case of a Dirac system, since the energies of the Landau levels go as $\sqrt{n}$, its nonequidistant Landau spectra can have a quantitative behavior different from that of a semi-Dirac system. For a large value of the flux ϕ such as $\phi = \phi_0/100$, the flatness of the energy bands is observed for both the semi-Dirac and Dirac systems owing to the shrinking of the cyclotron radius [see Figs. 5(a) and 5(e)]. The energy bands become parabolic for $\phi = \phi_0/200$, as seen from Fig. 5(b). The flatness of the Landau spectrum in the bulk completely vanishes in the semi-Dirac system compared to a Dirac one [see Figs. 5(b) and 5(f)]. With lower values of ϕ/ϕ_0, the Landau levels demonstrate a dispersive behavior and start getting flatter for large values of n for $t_2 = 2t$ [see Fig. 5(c)]. In the case of a Dirac system ($t_2 = t$), the Landau levels show quite a distinct behavior, where the flat bands become dispersive in the bulk, corresponding to larger values of n and lower values of ϕ/ϕ_0 [see Fig. 5(g)]. For a small value of the magnetic field, such that the flux is given by $\phi = \phi_0/1600$, the energy bands eventually become flat in the bulk for the semi-Dirac case, as shown in Fig. 5(d). This is not the case for a Dirac system [see Fig. 5(h)]. For all values of ϕ/ϕ_0, the zero-energy mode is completely separated from the bulk bands for a semi-Dirac system compared to the Dirac case (see any of the panels in Fig. 5).

IV. TRANSPORT PROPERTIES

To study the transport properties in the presence of a perpendicular magnetic field, we consider a large sample of a lattice model of the semi-Dirac system consisting of millions of atoms. The contribution to transport comes from both the off-diagonal and diagonal terms that appear in the Kubo formula [43]. The former contributes to the Hall conductivity σ_{xy}, whereas the latter leads to individual longitudinal conductivity in different directions (σ_{xx} and σ_{yy}).

A. Methodology

In this section, we shall describe the numerical approach developed by Garcia and coworkers [38], which is based on a real-space implementation of the Kubo formalism, where both the diagonal and off-diagonal conductivities are treated on the same footing. It is known that in momentum space, the Hall conductivity can be easily obtained in terms of the Berry curvature associated with the bands [44]. The Kubo formalism can be implemented in real space to obtain the Hall conductivity [38], which uses Chebyshev expansions to compute the conductivities. The components of the dc conductivity tensor ($\omega \to 0$ limit of the ac conductivity) for the noninteracting electrons are given by the Kubo-Bastin formula [43,45], which can be written as [38,46,47]

$$\sigma_{\alpha\beta}(\mu, T) = \frac{ie^2\hbar}{A}\int_{-\infty}^{\infty} d\varepsilon f(\varepsilon)\mathrm{Tr}\Big\langle v_\alpha \delta(\varepsilon - H) v_\beta \frac{dG^+(\varepsilon)}{d\varepsilon} - v_\alpha \frac{dG^-(\varepsilon)}{d\varepsilon} v_\beta \delta(\varepsilon - H)\Big\rangle, \quad (6)$$

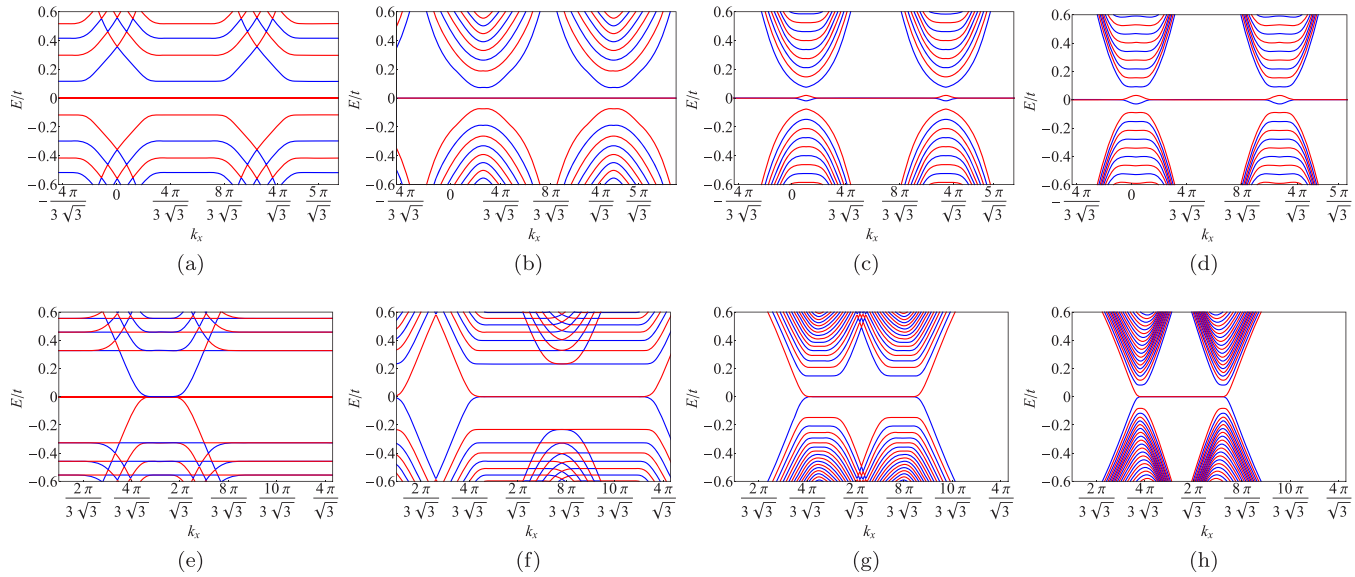

FIG. 5. Evolution of Landau levels for a finite strip with $N = 100$ unit cells in the presence of a magnetic flux $\phi = \frac{\phi_0}{100}, \frac{\phi_0}{200}, \frac{\phi_0}{500}$, and $\frac{\phi_0}{1600}$ for (a)–(d) $t_2 = 2t$ (semi-Dirac) and (e)–(h) $t_2 = t$ (Dirac).

where T is the temperature, μ is the chemical potential, v_α is the α component of the velocity operator, A is the area of the sample, $f(\varepsilon)$ is the Fermi-Dirac distribution, and $G^{\pm}(\varepsilon, H) = \frac{1}{\varepsilon - H \pm i\eta}$ are the advanced (+) and retarded (−) Green's functions. Using the kernel polynomial method (KPM) [48], the rescaled δ and Green's functions can be expanded in terms of the Chebyshev polynomials; hence, Eq. (6) becomes

$$\sigma_{\alpha\beta}(\mu, T) = \frac{4e^2\hbar}{\pi A}\frac{4}{(\Delta E)^2}\int_{-1}^{1} d\tilde{\varepsilon}\frac{f(\tilde{\varepsilon})}{(1-\tilde{\varepsilon}^2)^2}\sum_{m,n}\Gamma_{nm}(\tilde{\varepsilon})\mu_{nm}^{\alpha\beta}(\tilde{H}), \tag{7}$$

where ΔE is the range of the energy spectrum, $\tilde{\varepsilon}$ is the rescaled energy whose upper and lower bounds are $+1$ and -1, respectively, and $\tilde{H}$ is the rescaled Hamiltonian. $\Gamma_{nm}(\tilde{\varepsilon})$ and $\mu_{nm}^{\alpha\beta}(\tilde{H})$ are functions of the rescaled energy and the Hamiltonian, respectively. The energy-dependent scalar function $\Gamma_{nm}(\tilde{\varepsilon})$ can be written as

$$\begin{aligned}\Gamma_{nm}(\tilde{\varepsilon}) \equiv\ & (\tilde{\varepsilon} - \mathrm{i}n\sqrt{1-\tilde{\varepsilon}^2})e^{\mathrm{i}n\arccos(\tilde{\varepsilon})}T_m(\tilde{\varepsilon}) \\ & + (\tilde{\varepsilon} + \mathrm{i}m\sqrt{1-\tilde{\varepsilon}^2})e^{-\mathrm{i}m\arccos(\tilde{\varepsilon})}T_n(\tilde{\varepsilon}),\end{aligned} \tag{8}$$

and the Hamiltonian-dependent term which involves products of polynomial expansions can be written as

$$\mu_{nm}^{\alpha\beta}(\tilde{H}) = \frac{g_m g_n}{(1+\delta_{n0})(1+\delta_{m0})}\mathrm{Tr}[v_\alpha T_m(\tilde{H}) v_\beta T_n(\tilde{H})], \tag{9}$$

where the Chebyshev polynomials $T_m(x)$ obey the recurrence relation,

$$T_m(x) = 2xT_{m-1}(x) - T_{m-2}(x). \tag{10}$$

The Jackson kernel g_m is used to smoothen out the Gibbs oscillations which arise due to the truncation of the expansion in Eq. (7) [48,49]. The DOS can be calculated using an efficient algorithm based on the evolution of the time-dependent Schrödinger equation. We use a random superposition of all basis states as an initial state $|\phi(0)\rangle$,

$$|\phi(0)\rangle = \sum_i a_i |i\rangle, \tag{11}$$

where $|i\rangle$ denote the basis states and a_i are the normalized random complex numbers. Applying the Fourier transformation to the correlation function $\langle\phi(0)|e^{-iHt}|\phi(0)\rangle$, we get the DOS

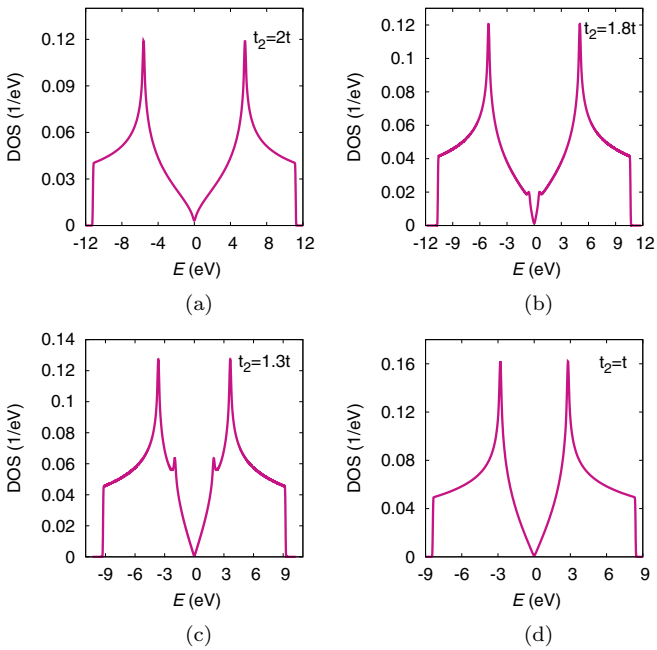

FIG. 6. The density of states (in units of 1/eV) is plotted as a function of energy E (in eV) for (a) $t_2 = 2t$ (semi-Dirac), (b) $t_2 = 1.8t$, (c) $t_2 = 1.3t$, and (d) $t_2 = t$ (Dirac). We set $t = 2.8$ eV in the calculation.

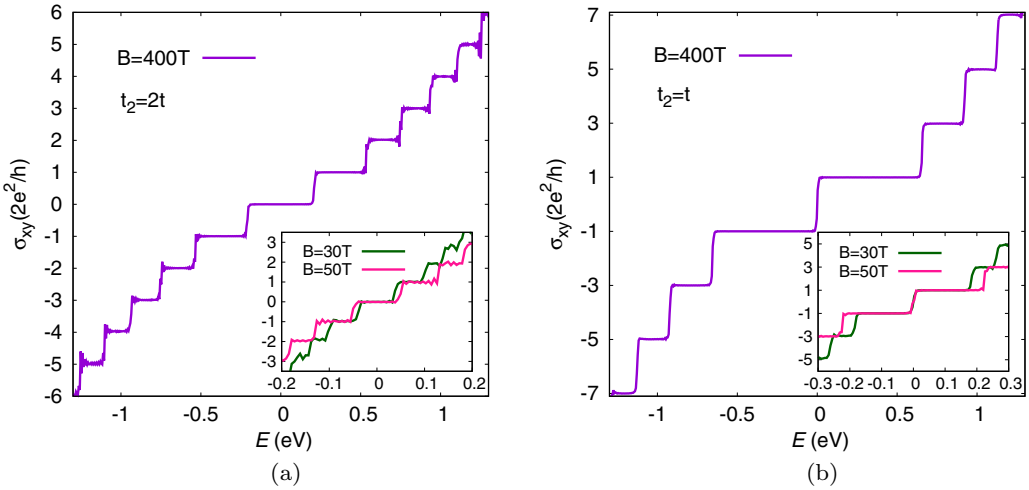

FIG. 7. The Hall conductivity σ_{xy} (in units of $2e^2/h$) is plotted as a function of Fermi energy E (in eV) for (a) $t_2 = 2t$ (semi-Dirac) and (b) $t_2 = t$ (Dirac) for a very high field (400 T) and a moderate field (30 and 50 T). Here t is taken to be 2.8 eV.

as [36]

$$\mathrm{DOS} = \frac{1}{2\pi}\int_{-\infty}^{\infty} e^{i\epsilon t}\langle\phi(0)|e^{-iHt}|\phi(0)\rangle dt, \qquad (12)$$

where t denotes time.

B. Longitudinal and Hall conductivities

Using the above-mentioned efficient numerical approach, we calculate the DOS in the absence and the presence of a magnetic field, the longitudinal conductivity in both the x (σ_{xx}) and y (σ_{yy}) directions, and the Hall conductivity σ_{xy} for the semi-Dirac system ($t_2 = 2t$). To compare the Dirac and semi-Dirac systems, we also show results for the Dirac ($t_2 = t$) case simultaneously. In our simulation, we consider a lattice of 5120 unit cells in each of the x and y directions [that is, a sample size denoted by (L_x, L_y) as (5120, 5120)]. We apply periodic boundary conditions for all our numerical results. We set the nearest-neighbor hopping parameter $t = 2.8$ eV. We adopt a large number of Chebyshev moments M since the energy resolution of the KPM and the convergence of the peaks of σ_{xx} depend on M. We use $M = 6144$ here [38]. The system size and the truncation order can be enhanced to reduce the fluctuations.

To get a feel for the evolution of the single-particle properties between the Dirac and semi-Dirac limits, we plot the DOS in the absence of a magnetic field for different values of t_2 in Fig. 6. In the case of a semi-Dirac system ($t_2 = 2t$), the DOS is proportional to $\sqrt{|E|}$ near $E \simeq 0$ [see Fig. 6(a)], while for the Dirac case ($t_2 = t$), again near zero energy the DOS varies as $|E|$, as shown in Fig. 6(d). In the two intermediate values of t_2, namely, $t_2 = 1.8t$ and $t_2 = 1.3t$ [as shown in Figs. 6(b) and 6(c)], a kink is visible near $E = 0$ which disappears for both the semi-Dirac and Dirac cases.

Next, we show the results for Hall conductivity σ_{xy} for moderate values of the magnetic field as well as extremely high fields in Fig. 7. Generally higher values of the magnetic field require a smaller system size, and hence, a smaller number of Chebyshev moments have to be computed. This yields faster convergence of the Hall conductivity in the limit of a large magnetic field. For $t_2 = 2t$ (semi-Dirac), the Hall conductivity σ_{xy} is plotted as a function of Fermi energy E for a large value of the field $B = 400$ T [as shown in the main frame of Fig. 7(a)]. To relate this result to recent experiments [50–52] performed for realistic values of magnetic field on a Dirac system, we also plot the Hall conductivity for moderate values of the field, namely, 30 T (green curve) and 50 T (pink curve), as shown in the inset of Fig. 7(a). The quantization of the plateaus is similar to that of a conventional 2DEG with a parabolic band dispersion in the sense that the conductance quantization happens at $\sigma_{xy} = 2ne^2/h$, where n takes integer values 0, ±1, ±2, ±3, ±4, ... in units of $2e^2/h$. The plot in the inset shows that the plateau step can be obtained with good accuracy even in the case of realistic values of the magnetic field. The difference between the semi-Dirac and Dirac cases lies in the fact that the fluctuations in the plateau step become prominent with the lowering of the field, especially at higher values of the Fermi energy. Further lowering of the magnetic field will reduce the sharpness of the plateaus due to the effect of the finite energy resolution and finite size of the sample. These are the artifacts of the method used here. In the Dirac system ($t_2 = t$), the well-known Hall quantization at $\sigma_{xy} = 2(2n+1)e^2/h$ is observed for very high magnetic field, namely, $B = 400$ T, as shown in the main frame of Fig. 7(b). The inset shows the same for realistic values of the magnetic field. The Hall conductivity plot ensures that there is a transition from a half-integer to an integer quantum Hall effect as we go from a Dirac to a semi-Dirac system by tuning t_2 [Figs. 7(a) and 7(b)]. The reason can be drawn from the fact that although the band dispersion in the semi-Dirac is linear in one direction, the quadratic behavior in the other direction seemingly dominates over the linear term, which results in a similar characteristic of conductance quantization of a 2DEG. In Fig. 8, we show the Hall conductivity σ_{xy} and the DOS for $B = 50$ and 400 T in the same frame. In the presence of the magnetic field, the DOS consists of peaks of discrete energy levels (Landau levels), as shown in Fig. 8. The DOS vanishes in the plateau region and shows a sharp peak corresponding to a Landau level when the

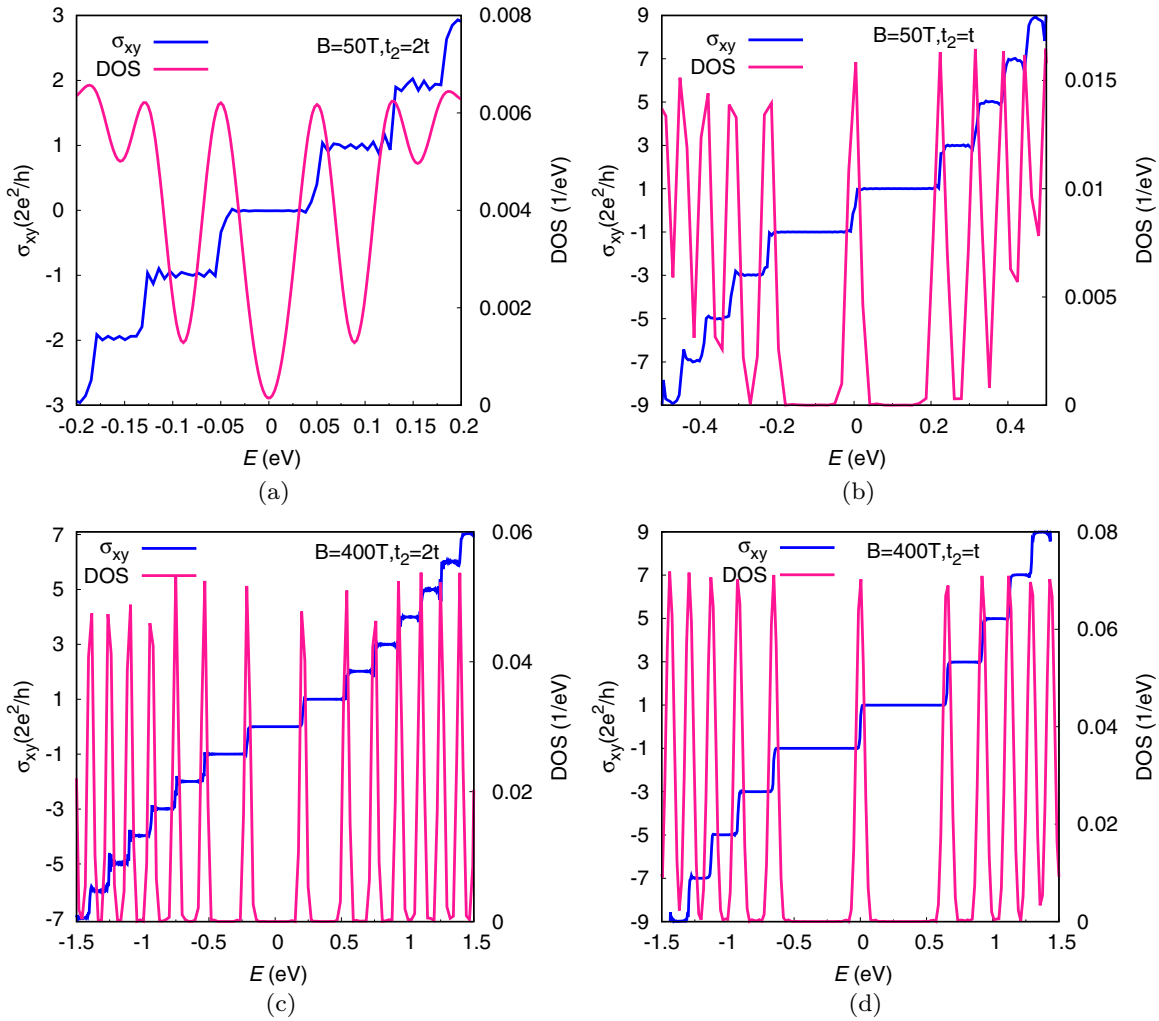

FIG. 8. The Hall conductivity σ_{xy} (in units of $2e^2/h$) and the DOS (in units of $1/\text{eV}$) are plotted as a function of Fermi energy E (in eV) for different cases: (a) $t_2 = 2t$, $B = 50\,\text{T}$, (b) $t_2 = t$, $B = 50\,\text{T}$, (c) $t_2 = 2t$, $B = 400\,\text{T}$, and (d) $t_2 = t$, $B = 400\,\text{T}$.

Hall conductivity goes through a transition from one plateau to another. However, we get broad DOS peaks at lower values of the magnetic field ($B = 50\,\text{T}$), which is particularly visible for the semi-Dirac case owing to the small energy separation between the Landau levels (less than 3 meV). Sharper peaks will require computation of a very large number of Chebyshev moments. Figure 8(a) shows that there is no Landau level peak at zero energy for $t_2 = 2t$, which is also characteristic of a conventional 2DEG, in contrast to the $t_2 = t$ case, where the zero-energy peak is well observed [see Fig. 8(b)]. The presence of a zero-energy peak for the Dirac case is related to the chiral anomaly present there. Figures 8(c) and 8(d) show that several Landau levels can be observed with the same qualitative behavior for very high magnetic field $B = 400\,\text{T}$ for both the semi-Dirac and Dirac systems. The Hall conductance is quantized due to the quantized Landau level. It is interesting to note that although the energy does not depend linearly on the Landau level index n and magnetic field B in the case of a semi-Dirac system, as stated earlier, the quantized value of σ_{xy} of a semi-Dirac material is analogous to that of a 2DEG. It is once again pertinent to mention that the Landau level spectra in phosphorene in a perpendicular magnetic field depending on the index n (an additional factor of 2 will appear for spin degeneracy) have connections to the semi-Dirac physics [34,35].

To investigate the magnetotransport, we further calculate the longitudinal conductivity along the x (σ_{xx}) and y (σ_{yy}) directions. Figures 9(a) and 9(b) show the longitudinal conductivities σ_{xx} (green curve) and σ_{yy} (magenta curve) as a function of the Fermi energy E for moderate values of the B field $B = 50\,\text{T}$ for a semi-Dirac and a Dirac system, respectively. The longitudinal conductivity reveals largely anisotropic behavior owing to the presence of anisotropy in the dispersion for $t_2 = 2t$. The components of σ in the x (σ_{xx}) and y (σ_{yy}) directions are quantitatively different in nature. The magnitude of σ_{yy} is larger than that of σ_{xx}. This is definitely a contrasting feature compared to the case of a Dirac system where the magnitudes of σ_{xx} and σ_{yy} are the same, as shown in Fig. 9(b). Moreover, the absence of a zero-energy peak also supports our discussion of the Landau level results [see Fig. 8(c)] for the semi-Dirac material. Figures 9(c) and 9(d) show similar results for very high values of the magnetic field, namely, $B = 400\,\text{T}$, with the

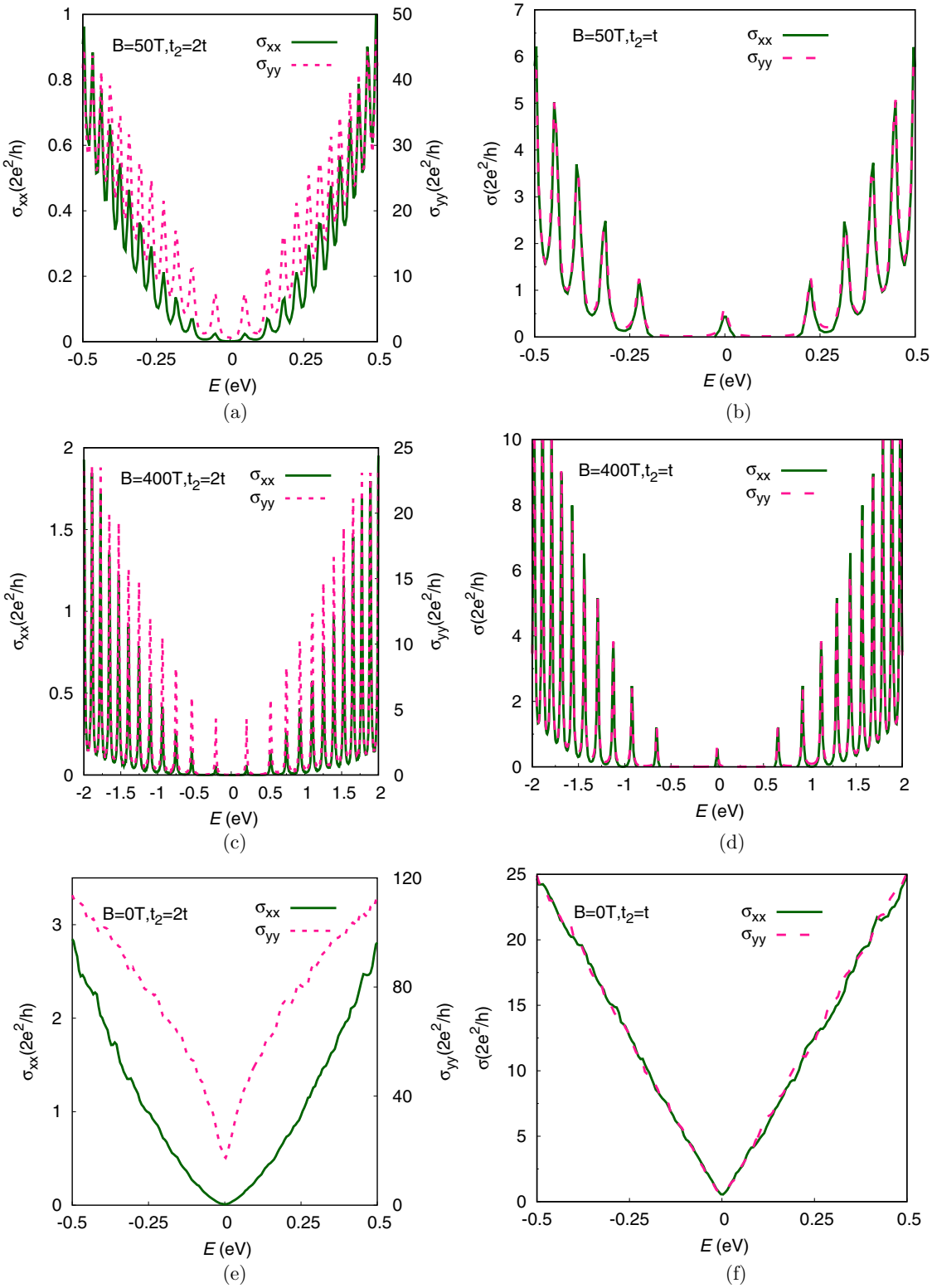

FIG. 9. Longitudinal conductivities σ_{xx} and σ_{yy} (in units of $2e^2/h$) are plotted as a function of Fermi energy E (in eV) for different cases: (a) $t_2 = 2t$, $B = 50\,\mathrm{T}$, (b) $t_2 = t$, $B = 50\,\mathrm{T}$, (c) $t_2 = 2t$, $B = 400\,\mathrm{T}$, (d) $t_2 = t$, $B = 400\,\mathrm{T}$, (e) $t_2 = 2t$, $B = 0\,\mathrm{T}$, and (f) $t_2 = t$, $B = 0\,\mathrm{T}$.

well-observed sharp peaks at larger values of energy. The amplitudes increase at large values of the Fermi energy owing to the increase in the scattering rate of the Landau levels as one goes to higher values of n for both the semi-Dirac and Dirac systems. Since the Landau levels are not equidistant for both cases, the interval between the peaks is not spaced equally. It can be seen that the longitudinal conductivity is nonvanishing only when the Fermi energy is within a Landau band where the backscattering processes are present.

To compare and contrast further between the two cases, we plot the longitudinal conductivities (σ_{xx} and σ_{yy}) in the absence of any magnetic field ($B = 0$) in Figs. 9(e) and 9(f) for the semi-Dirac and Dirac systems, respectively. Apart from the suppression of the conductivities by one order of magnitude by the magnetic field, one can note the linear dependence of the conductivity on the Fermi energy E for the Dirac case [31,53], while the conductivity as a function of E appears with a different exponent for the semi-Dirac one. The feature is qualitatively the same as that observed for $B \neq 0$. However, the peaks in the conductance spectra vanish at $B = 0$ owing to the absence of Landau levels.

V. SUMMARY

In this work, we have studied the influence of a perpendicular magnetic field with a semi-Dirac dispersion within the framework of a tight-binding model of a honeycomb lattice. In order to compare and contrast with a prototype Dirac material, such as graphene, we have presented our results for both cases. We considered a semi-Dirac nanoribbon with a finite width and studied the Hofstadter's butterfly and properties of the Landau level spectra. We have observed two identical gapped spectra symmetrically placed above and below $E = 0$ along with a zero-energy mode in the Hofstadter's butterfly spectrum, in contrast to what is observed for a Dirac system. The Landau level becomes fully dispersive in the bulk for moderate values of the magnetic flux, which is not true for the Dirac case. Furthermore, we explore the magnetotransport properties using the Kubo formula. We observed that the Hall conductivity shows standard quantization similar to that of a conventional semiconductor 2DEG with a parabolic band, which is highly contrasted with respect to a Dirac system. The zero Landau level peak is absent in the case of a semi-Dirac system. The longitudinal conductivities σ_{xx} and σ_{yy} show anisotropic behavior due to the distinct dispersion in two longitudinal directions.

ACKNOWLEDGMENTS

P.S. acknowledges S. M. João, SK Firoz Islam, A. Adel for useful discussions and R. Rahaman for helping with computation. S.B. thanks SERB, India, for financial support under Grant No. EMR/2015/001039. S.M. is supported by JSPS KAKENHI under Grant No. JP18H03678.

[1] P. R. Wallace, Phys. Rev. **71**, 622 (1947).
[2] A. H. Castro Neto, F. Guinea, N. M. R. Peres, K. S. Novoselov, and A. K. Geim, Rev. Mod. Phys. **81**, 109 (2009).
[3] L. Pauling, Proc. Natl. Acad. Sci. USA **56**, 1646 (1966).
[4] L. Tarruell, D. Greif, T. Uehlinger, G. Jotzu, and T. Esslinger, Nature (London) **483**, 305 (2012).
[5] P. Dietl, F. Piéchon, and G. Montambaux, Phys. Rev. Lett. **100**, 236405 (2008).
[6] S. Banerjee, R. R. P. Singh, V. Pardo, and W. E. Pickett, Phys. Rev. Lett. **103**, 016402 (2009).
[7] A. S. Rodin, A. Carvalho, and A. H. Castro Neto, Phys. Rev. Lett. **112**, 176801 (2014).
[8] J. Guan, Z. Zhu, and D. Tománek, Phys. Rev. Lett. **113**, 046804 (2014).
[9] A. N. Rudenko, S. Yuan, and M. I. Katsnelson, Phys. Rev. B **92**, 085419 (2015).
[10] C. Dutreix, E. A. Stepanov, and M. I. Katsnelson, Phys. Rev. B **93**, 241404(R) (2016).
[11] V. Pardo and W. E. Pickett, Phys. Rev. Lett. **102**, 166803 (2009).
[12] V. Pardo and W. E. Pickett, Phys. Rev. B **81**, 035111 (2010).
[13] G. Montambaux, F. Piéchon, J.-N. Fuchs, and M. O. Goerbig, Phys. Rev. B **80**, 153412 (2009).
[14] Y. Hasegawa, R. Konno, H. Nakano, and M. Kohmoto, Phys. Rev. B **74**, 033413 (2006).
[15] Y. Suzumura, T. Morinari, and F. Pichon, J. Phys. Soc. Jpn. **82**, 023708 (2013).
[16] J. Kim, S. S. Baik, S. H. Ryu, Y. Sohn, S. Park, B. G. Park, J. Denlinger, Y. Yi, H. J. Choi, and K. S. Kim, Science **349**, 723 (2015).
[17] C. Si, Z. Sun, and F. Liu, Nanoscale **8**, 3207 (2016).
[18] J. Zhao, H. Liu, Z. Yu, R. Quhe, S. Zhou, Y. Wang, C. C. Liu, H. Zhong, N. Han, J. Lu, Y. Yao, and K. Wu, Prog. Mater. Sci. **83**, 24 (2016).
[19] P. Vogt, P. DePadova, C. Quaresima, J. Avila, E. Frantzeskakis, M. C. Asensio, A. Resta, B. Ealet, and G. Le Lay, Phys. Rev. Lett. **108**, 155501 (2012).
[20] L. Meng, Y. Wang, L. Zhang, S. Du, R. Wu, L. Li, Y. Zhang, G. Li, H. Zhou, W. A. Hofer, and H. J. Gao, Nano Lett. **13**, 685 (2013).
[21] L. Li, S. Z. Lu, J. Pan, Z. Qin, Y. Q. Wang, Y. Wang, G. Y. Cao, S. Du, and H. J. Gao, Adv. Mater. **26**, 4820 (2014).
[22] F. F. Zhu, W. J. Chen, Y. Xu, C. L. Gao, D. D. Guan, C. H. Liu, D. Qian, S. C. Zhang, and J. F. Jia, Nat. Mater. **14**, 1020 (2015).
[23] A. Molle, C. Grazianetti, D. Chiappe, E. Cinquanta, E. Cianci, G. Tallarida, and M. Fanciulli, Adv. Funct. Mater. **23**, 4340 (2013).
[24] T. Morishita and M. J. Spencer, Sci. Rep. **5**, 17570 (2015).
[25] L. Zhang, P. Bampoulis, A. N. Rudenko, Q. Yao, A. van Houselt, B. Poelsema, M. I. Katsnelson, and H. J. W. Zandvliet, Phys. Rev. Lett. **116**, 256804 (2016).
[26] V. O. Özçelik, S. Cahangirov, and S. Ciraci, Phys. Rev. Lett. **112**, 246803 (2014).
[27] V. P. Gusynin and S. G. Sharapov, Phys. Rev. Lett. **95**, 146801 (2005).
[28] Y. Zheng and T. Ando, Phys. Rev. B **65**, 245420 (2002).
[29] Y. Zhang, Y. W. Tan, H. L. Stormer, and P. Kim, Nature (London) **438**, 201 (2005).
[30] K. S. Novoselov, Z. Jiang, Y. Zhang, S. V. Morozov, H. L. Stormer, U. Zeitler, J. C. Maan, G. S. Boebinger, P. Kim, and A. K. Geim, Science **315**, 1379 (2007).
[31] K. S. Novoselov, A. K. Geim, S. V. Morozov, D. Jiang, M. I. Katsnelson, I. V. Grigorieva, S. V. Dubonos, and A. A. Firsov, Nature (London) **438**, 197 (2005).
[32] P. Plochocka, C. Faugeras, M. Orlita, M. L. Sadowski, G. Martinez, M. Potemski, M. O. Goerbig, J.-N. Fuchs, C. Berger, and W. A. de Heer, Phys. Rev. Lett. **100**, 087401 (2008).

[33] M. L. Sadowski, G. Martinez, M. Potemski, C. Berger, and W. A. de Heer, Phys. Rev. Lett. **97**, 266405 (2006).
[34] X. Y. Zhou, R. Zhang, J. P. Sun, Y. L. Zou, D. Zhang, W. K. Lou, F. Cheng, G. H. Zhou, F. Zhai, and K. Chang, Sci. Rep. **5**, 12295 (2015).
[35] S. Yuan, E. van Veen, M. I. Katsnelson, and R. Roldan, Phys. Rev. B **93**, 245433 (2016).
[36] S. Yuan, H. De Raedt, and M. I. Katsnelson, Phys. Rev. B **82**, 115448 (2010).
[37] S. Yuan, T. O. Wehling, A. I. Lichtenstein, and M. I. Katsnelson, Phys. Rev. Lett. **109**, 156601 (2012).
[38] J. H. Garcia, L. Covaci, and T. G. Rappoport, Phys. Rev. Lett. **114**, 116602 (2015).
[39] K. Saha, Phys. Rev. B **94**, 081103(R) (2016).
[40] Q. Chen, L. Du, and G. A. Fiete, Phys. Rev. B **97**, 035422 (2018).
[41] SK Firoz Islam and A. Saha, Phys. Rev. B **98**, 235424 (2018).
[42] R. Rammal, J. Phys. **46**, 1345 (1985).
[43] R. Kubo, J. Phys. Soc. Jpn. **12**, 570 (1957).
[44] D. J. Thouless, M. Kohmoto, M. P. Nightingale, and M. den Nijs, Phys. Rev. Lett. **49**, 405 (1982).
[45] R. Kubo, A. Yokota, and S. Nakajima, J. Phys. Soc. Jpn. **12**, 1203 (1957).
[46] A. Bastin, C. Lewiner, O. Betbeder-Matibet, and P. Nozieres, J. Phys. Chem. Solids **32**, 1811 (1971).
[47] F. Ortmann, N. Leconte, and S. Roche, Phys. Rev. B **91**, 165117 (2015).
[48] A. Weisse, G. Wellein, A. Alvermann, and H. Fehske, Rev. Mod. Phys. **78**, 275 (2006).
[49] R. N. Silvera, H. Roederb, A. F. Votera, and J. D. Kressb, J. Comput. Phys. **124**, 115 (1996).
[50] A. F. Young, C. R. Dean, L. Wang, H. Ren, P. Cadden-Zimansky, K. Watanabe, T. Taniguchi, J. Hone, K. L. Shepard, and P. Kim, Nat. Phys. **8**, 550 (2012).
[51] C. R. Dean, L. Wang, P. Maher, C. Forsythe, F. Ghahari, Y. Gao, J. Katoch, M. Ishigami, P. Moon, M. Koshino *et al.*, Nature (London) **497**, 598 (2013).
[52] B. Hunt, J. D. Sanchez-Yamagishi, A. F. Young, M. Yankowitz, B. J. LeRoy, K. Watanabe, T. Taniguchi, P. Moon, M. Koshino, P. Jarillo-Herrero *et al.*, Science **340**, 1427 (2013).
[53] M. Novak, S. Sasaki, K. Segawa, and Y. Ando, Phys. Rev. B **91**, 041203(R) (2015).